Faraday Discussions

Cite this: DOI: 10.1039/d6fd00045b

PAPER

Published on 18 August 2026

Multiscale testing of mechanical properties of lithium anodes in conventional electrolytes in comparison to ionic liquids

Beatrice Wolff, †*[ab] Sascha Berg, †*[c] Alexander Pinto,[d] Tobias Sedlatschek, [ef] Xinlin Li, [g] Ziyuan Lyu, [hi] Dominik Stępień, [hi] Christoph Broeckmann, [ef] Dominic Bresser, [hij] Rüdiger-A. Eichel, [abk] Chi-Cheung Su, [g] Egbert Figgemeier [cd] and Florian Hausen *[ab]

Received 10th March 2026, Accepted 7th April 2026

DOI: 10.1039/d6fd00045b

The mechanical properties of a solid–electrolyte interphase (SEI), such as hardness and Young's modulus, influence the ion transport pathways through the SEI as well as affecting the dendrite formation processes. Moreover, the local composition of the SEI has a strong influence on mechanical variations at small scales, making a thorough understanding of such properties with high detail in depth and with high spatial resolution crucial. Within this contribution, *in operando* atomic force microscopy (AFM) and nanoindentation are used to investigate the mechanical properties of the SEI in conventional electrolytes in comparison to those in ionic liquids. While both methods have been shown to be powerful tools to investigate SEI formation, distinctive mechanical fingerprints are demonstrated for SEIs formed in carbonate electrolytes on lithium deposited on copper in AFM-based experiments. Such fingerprints change significantly when ionic liquids are used as electrolytes and depend critically on the exact composition. These results are correlated with nanoindentation, performed on

[a]*Institute of Energy Technologies, IET-1 - Forschungszentrum Jülich, Jülich, Germany. E-mail: b.wolff@fz-juelich.de; f.hausen@fz-juelich.de*

[b]*Institute of Physical Chemistry, RWTH Aachen University, Aachen, Germany*

[c]*Helmholtz-Institute Münster (HIMS): Ionics in Energy Storage, IMD-4– Forschungszentrum Jülich, Aachen, Germany. E-mail: s.berg@fz-juelich.de*

[d]*Institute of Power Electronics and Electrical Drives (ISEA), RWTH Aachen University, Aachen, Germany*

[e]*Institute for Materials Applications in Mechanical Engineering (IWM), RWTH Aachen University, Aachen, Germany*

[f]*Institute of Applied Powder Metallurgy and Ceramics at RWTH Aachen e.V., Aachen, Germany*

[g]*Chemical Sciences and Engineering Division, Argonne National Laboratory, Lemont, USA*

[h]*Helmholtz Institute Ulm (HIU), Ulm, Germany*

[i]*Karlsruhe Institute of Technology (KIT), Karlsruhe, Germany*

[j]*Ulm University, Ulm, Germany*

[k]*Faculty of Mechanical Engineering, RWTH Aachen University, Aachen, Germany*

† These authors contributed equally.

freshly cleaved lithium surfaces in an inert atmosphere and carbonate solvents. Additionally, lithium surfaces treated with varying amounts of and exposure times to ionic liquids are studied. In both cases, AFM-based experiments and nanoindentation, higher stiffnesses and storage moduli are found, indicating a highly complex SEI structure.

Introduction

The solid–electrolyte interphase (SEI) formed on Li-metal anodes in combination with liquid non-aqueous electrolytes is one of the most important features governing the longevity, safety and performance of lithium metal batteries (LMBs).[1,2] Li metal[3] as the active material in anode-free concepts is deposited and stripped, resulting in severe morphological and volumetric changes. The SEI as a heterogeneous composition of organic and inorganic components needs to be flexible enough to withstand these changes without cracking and decomposition. Additionally, it needs to completely cover the Li-metal surface as an interphase in order to ensure stability between the electrode and the electrolyte. The mixed SEI structure of organic and inorganic species (*e.g.*, Li_2CO_3, LiF and polymeric decomposition products) formed in carbonate-based electrolytes provides great longevity and safety when graphite anodes are used, but low cycle life and safety issues occur with Li-metal anodes.[3] A promising step towards designing an SEI that stabilises the Li-metal surface against the liquid electrolyte is the use of ionic liquid (IL)-based electrolytes.[2] The IL cation chemistry allows it to be engineered for generating self-forming artificial SEI (ASEI) layers with certain compositions of inorganic phases, such as LiF and Li_3N, in a more uniform and stratified structure that is stiffer than that of their inorganic counterparts and might therefore contribute to the suppression of the formation of dendritic structures.[4] Superconcentrated IL-based electrolytes (*e.g.*, 3.2 mol per kg LiTFSI in pyrrolidinium(Pyr) cations) were shown to form thick, uniform and inorganic-rich SEI layers with enhanced cycling stability with Li metal.[5] Also pre-treatment of the Li-metal surface with gelled IL-based solutions was shown to form protective, polymer-like layers that are maintained on the Li-metal surface even during cycling with carbonate-based electrolytes.[6]

Ion transport pathways through the SEI, the surface morphology and especially the suppression of dendrite formation are directly influenced by the mechanical properties of the SEI, in particular its Young's modulus, hardness and viscoelastic behavior. Nanoindentation and atomic force microscopy (AFM) are suitable methods for the analysis of mechanical properties.[7–9] However, despite its importance, reports about the experimental mechanical characterisation of the SEI on Li metal are scarce.[10–14]

The SEI also plays an important role in batteries with anode materials other than Li metal. Both AFM and nanoindentation have also been used to study the mechanical properties of the SEI formed on other anode materials[15] such as graphite,[16] silicon,[17,18] K–Sb and Li–Sn micro-particles,[19] Na metal[20] and Zn metal.[21]

This work discusses the mechanical characterisation of the SEI by means of AFM and nanoindentation and how complementary these methods are. Quantitative nanomechanical mapping using AFM enables high spatial resolution in the nanometre range to probe the outermost SEI layer's surface morphology and

stiffness. As a non-destructive method, it is performed inside an electrochemical cell during operation and offers temporally resolved results. Because of the shallow probing depths of typically <50 nm in AFM experiments, only the topmost surface layers are probed.[11,22] In contrast, nanoindentation, especially when using continuous stiffness measurement (CSM), provides information about the mechanical properties of deeper structures,[23] revealing information about the layered architecture of the SEI. Oliver and Pharr illustrated quantitative determination of Young's modulus and hardness, which were directly comparable with literature values and computational predictions.[23,24] Here, the complementarity of AFM and nanoindentation is demonstrated for SEI properties in conventional and IL electrolytes for samples of Li deposited on Cu and Li-metal foil. In a first section, mechanical properties obtained by *in operando* AFM experiments are directly compared to those recorded by *ex situ* nanoindentation results. This is followed by a more detailed report of *in operando* AFM studies on Li deposited on Cu and on Li-metal in carbonate electrolytes for different deposition times. Subsequently, nanoindentation results on metallic Li are shown in carbonate electrolyte. After comparing their electrochemical performance to the same substrate being pretreated with ILs, nanoindentation of such pretreated Li surfaces are illustrated. Finally, mechanical properties obtained by *in operando* AFM on Li deposited on Ni-substrates are presented. The results discussed here provide a multiscale understanding of the mechanical parameters: AFM reveals fingerprints of the organic phases, while nanoindentation probes the mechanical properties of the heterogeneous SEI bulk.

Methods

For AFM measurements, we report values for surface stiffness, while we use the term elastic modulus for nanoindentation. Both terms refer to the mean Young's modulus for the probed depth. These different terms are used to illustrate how the probing depth of those two techniques changes the measured parameter although the physical quantity is different. Since the exact composition of the probed samples is unknown, we report reduced moduli.

Fig. 1 portrays an overview of AFM and nanoindentation and the corresponding workflows used in this work. A sketch illustrating the working principles is depicted in Fig. 1a. Nanoindentation indents the surface at single indents spaced apart, whereas AFM continuously indents the surface while scanning a small area. The nanoindentation workflow is displayed in Fig. 1b–e, whereas the atomic force microscopy workflow is depicted in Fig. 1f–j.

For nanoindentation, Li deposition on Cu was performed inside a coin cell with a special washer instead of a porous separator. The exploded-view drawing of the coin-cell setup is depicted in Fig. 1b. After the deposition was completed, the coin cell was disassembled inside a glovebox and the Cu foil with deposited Li metal was mounted on a scanning electron microscope (SEM) stub holder, used in the nanoindenter. Fig. 1c shows a photograph of the specific setup. Subsequently, the nanoindenter is transferred to the directly attached SEM chamber. Fig. 1d shows a wide-view SEM image of the surface of the deposited Li on Cu foil and the diamond tip used for indentation in the top part. During indentation, force and indentation depth are sampled. Contact stiffness, hardness and elastic

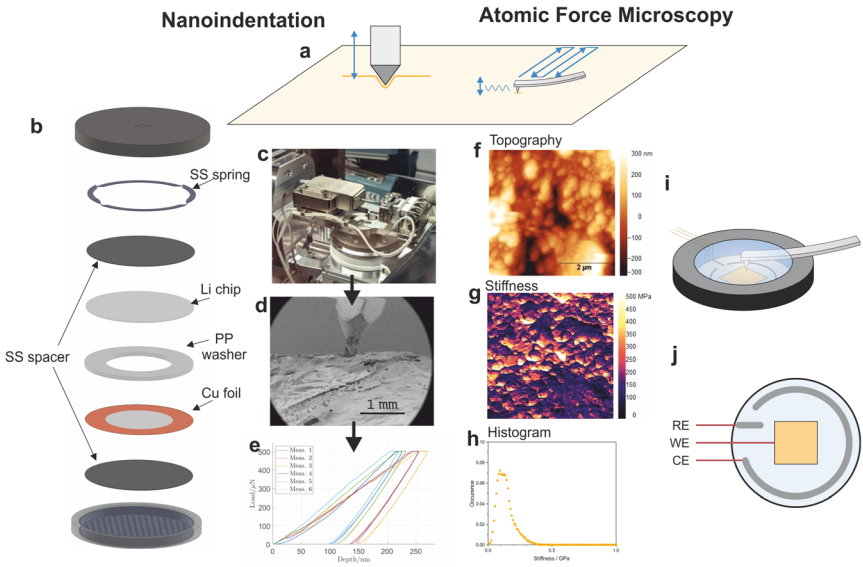

Fig. 1 Overview of the methods and workflows used in this work. (a) Sketch of the working principles of nanoindentation and atomic force microscopy. (b) Schematic depiction of the coin-cell setup for Li deposition on Cu foil. (c) Photo of the nanoindenter inside the glovebox with the attached indenter tip and sample tray. (d) Wide-view SEM image of the indenter above the surface of deposited Li. (e) Exemplary load–displacement curve obtained from indentation. (f) Topography map of Li deposited on Cu. (g) Stiffness map of Li deposited on Cu. (h) Corresponding stiffness histogram. (i) Schematic depiction of an electrochemical *in situ* AFM cell. (j) Schematic depiction of the electrode setup in the electrochemical *in situ* AFM cell with the working electrode (WE), counter electrode (CE) and reference electrode (RE).

modulus are then evaluated from the force-indentation depth curve, as can be seen in Fig. 1e, using the Oliver–Pharr method.[24]

AFM obtains the topography of the sample simultaneously to the mechanical properties of its surface. Fig. 1f shows the topography of Li deposited on Cu foil. The corresponding stiffness map is shown in Fig. 1g. For a more quantitative analysis and better comparability, the stiffness map is converted into a histogram, as demonstrated in Fig. 1h.

The experimental setup of the AFM is displayed in Fig. 1i and j. Fig. 1i shows a sketch of the electrochemical *in situ* AFM cell used for measurements. Experiments are conducted in a liquid environment while Li is plated onto the working electrode. A schematic depiction of the electrode setup inside the electrochemical AFM cell is provided in Fig. 1j. The sample is acting as the working electrode (WE). A Li counter electrode (CE) circumferences the working electrode while a Li reference electrode (RE) is placed at the edge of the cell.

However, the exact sample preparation for the two measurement techniques differs for both setups. AFM experiments were performed in liquid electrolyte during Li deposition on a Cu or Ni surface or on Li foil soaking in liquid electrolyte. Nanoindentation was performed on *ex situ* samples in a vacuum. These included electrodeposited Li on Cu, Li surfaces prepared by precise cutting in a controlled environment and Li surfaces treated with IL.

A more detailed description of both methods, relevant calibration procedures and experimental parameters is provided in the SI.

Results and discussion

Li on Cu – AFM and nanoindentation

The aim of this section is to demonstrate the complementarity of AFM and nanoindentation in 1–1.2 M $LiPF_6$ in ethyl carbonate/ethyl methyl carbonate (EC/EMC 3 : 7 by weight).

The mechanical properties of the SEI formed on Li deposited on a Cu surface were obtained *via* both AFM and nanoindentation. The AFM experiments were performed in electrolyte, during Li deposition. AFM obtains the localised elastic modulus of the surface at every pixel of the image scan. Since the modulus is defined as a bulk property, the measured value here is denoted as (surface) stiffness. Fig. 2 displays the elastic modulus determined for the SEI formed on Li deposited on Cu *via* both AFM and nanoindentation. AFM obtains locally resolved stiffness maps, converted to a histogram, consisting of $256 \times 256 = 65\,536$ individual measurements. These are displayed as histograms in Fig. 2.

As illustrated in Fig. 2a, the stiffness values obtained *via* AFM are mostly below 2 GPa. Fig. 2b shows a zoom into this smaller region. The stiffness histograms obtained *via* AFM differ in their shape, exhibiting different peaks with maxima at about 100 MPa, 160 MPa, 350 MPa and 400–800 MPa. The stiffness histograms are in a comparable range to those observed for the SEI on Li in a vitrified state, as reported by Zhang *et al.*[12] The organic part of the SEI on highly oriented pyrolytic graphite (HOPG) has been reported to exhibit a stiffness on the order of 0.5 GPa to 2 GPa,[25] a value that is found here as well.

For instrumental reasons described in the SI in more detail, the nanoindentation experiments were performed on disassembled samples of deposited Li, with two different resting times of 1 hour and 1 month. Nanoindentation

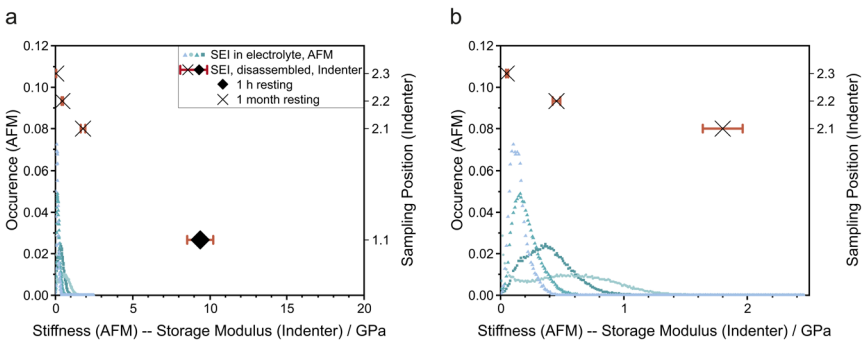

Fig. 2 Stiffness histograms obtained *via* AFM and storage modulus obtained *via* nanoindentation. AFM data were obtained in electrolyte during Li plating on Cu. Nanoindentation data were obtained at different areas of disassembled cells with Li plated on Cu. At least five measurements were recorded and averaged. Variation from average value is depicted as error bars. The sampling position describes the sample number and measurement position of the nanoindentation measurements. (a) AFM and nanoindentation data of the surface layer on Li deposited on Cu. (b) Close up of region 0–2.5 GPa.

provides the storage and loss modulus of the sample surface. In the case of a loss modulus close to zero, the storage modulus reflects the elastic modulus.

At least five indentations have been performed on each surface area. The mean value is depicted in Fig. 2, where error bars reflect the deviation of the individual values. Fig. 2b provides a closer look into the area between 0 and 2.5 GPa. Nanoindentation was performed on two different samples. One sample was rested for 1 h after cell opening (marked by X), the other sample was rested for 1 month (marked by a ◆). Interestingly, the nanoindentation results vary strongly between different sample positions, emphasising the importance of local understanding of the mechanical properties of the SEI. The values of the long-rested sample are below 2 GPa, while the short-rested sample exhibits a higher value of 9.4 GPa.

Overall, there is a good agreement between the AFM and nanoindentation results. Taking a closer look at the nanoindentation results in Fig. 2b, two sampling regions result in storage moduli of 50 MPa and 450 MPa, which are comparable to the stiffness values obtained *via* AFM. Similarly to the narrow AFM histograms, the nanoindentation results exhibit a low variance of storage modulus. The other nanoindentation sampling region (2.1) results in a storage modulus around 1.8 GPa, which is slightly higher than the stiffness values observed *via* AFM. Similarly to the broader distributions observed *via* AFM at higher stiffness values, the nanoindentation results exhibit a higher variance of storage modulus. The slightly higher elastic moduli observed *via* nanoindentation are attributed to the different measurement environments between AFM and nanoindentation. This is also in agreement with Zhang *et al.* reporting a higher elastic modulus for the SEI on Li in a dried state compared to a vitrified state.[12] Moreover, the nanoindentation results show a difference in stiffness for different resting periods, where the longer resting period results in a softer surface layer. This result suggests that during the longer resting period, soft components form in the outer part of the SEI.

Importantly, when comparing the results of AFM and nanoindentation experiments, the different sampling depths of both methods must be taken into account. While AFM only probes the outermost layer of the SEI with an indentation depth of a few nm, nanoindentation indents several hundred nm into the sample. As the SEI consists of a layered structure,[26] different species are probed by AFM and nanoindentation. Theoretical calculations of the elastic properties of different SEI components using a force-field-based method have been reported by Shin *et al.*[25] Organic components were found to have elastic moduli of 2.4 GPa (PEO), 7.9 GPa (LiEC), 10.7 GPa (LiMC) and 21.9 GPa (Li_2EDC), whereas the calculated values of the inorganic compounds Li_2CO_3 and LiF range from 36 GPa to 135 GPa, depending on the exact crystallinity.[25] Therefore, the results recorded *via* AFM and nanoindentation in this work suggest that an organic layer or multiple thin inorganic layers were probed.

Since it is demonstrated that AFM and nanoindentation provide complementary results, in the following sections the focus is put on the individual contributions.

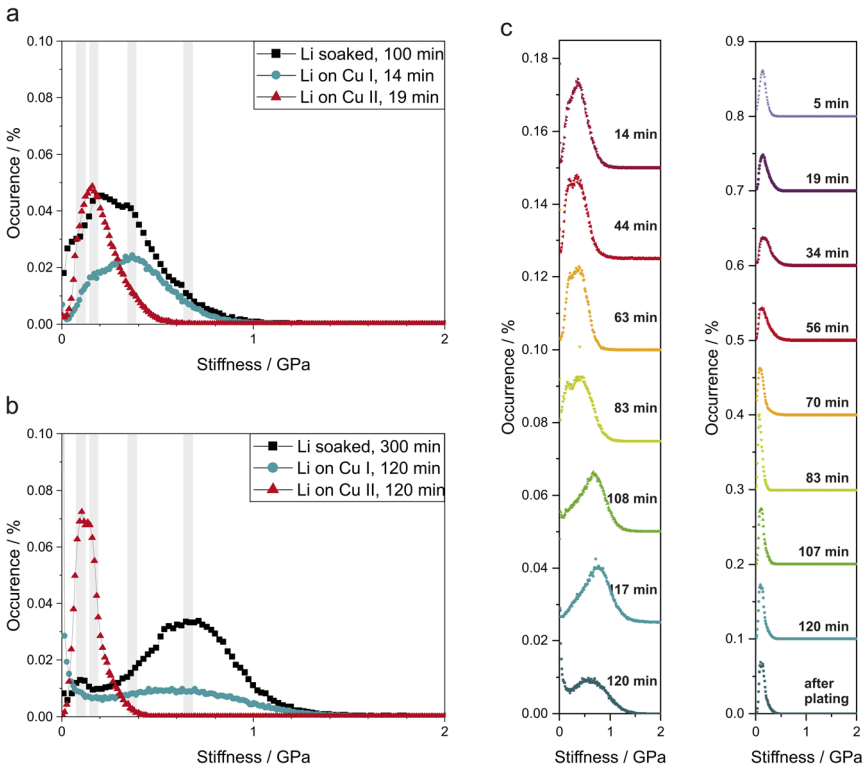

Fig. 3 Stiffness histograms of the outer SEI layer, obtained *via* AFM. (a and b) Stiffness histograms for the SEI formed on Li deposited on Cu and the SEI formed on Li foil soaked in electrolyte, with (a) short and (b) long durations of depositon or soaking. For SEI formation on deposited Li, two different experiments are shown (red and turquoise histograms). (c) *In situ* observation of SEI formation on deposited Li, for different plating durations. Two different experiments are shown.

Atomic force microscopy

Within this section, a closer look at the stiffness histograms obtained *via* AFM is provided. In particular, the stiffness histograms of the SEI formed on freshly deposited Li are compared to the stiffness histograms of the SEI formed by soaking Li foil in electrolyte. Additionally, the evolution of the SEI over time is taken into account. Fig. 3a and b show the same stiffness histograms as in Fig. 2 for the SEI freshly formed on Li deposited on Cu foil. Furthermore, histograms of the SEI formed on the surface of lithium foil soaked in electrolyte are shown.

Fig. 3a displays stiffness histograms obtained for the SEI formed on Li deposited on Cu in two different experiments, after 14 min (turquoise) and 19 min (red) of Li deposition. The black histogram corresponds to the SEI on Li foil soaked in electrolyte for 100 min. The stiffness histograms exhibit a right-skewed shape which is also multimodal in several cases. The stiffness histograms are fitted using a combination of several Gaussians, indicating several mechanically different species contributing to the shape of the histogram.[11] In Fig. 3, light grey lines mark the central positions of contributing peaks as a guide to the eye. Although the stiffness histograms are not identical, it is seen that the same

components contribute to the shape of the stiffness histograms, indicating that the same mechanical species are present in the outermost layer of the observed surfaces, regardless of how the SEI was formed. Fig. 3b illustrates stiffness histograms of the SEI for a longer Li deposition or soaking time in electrolyte. Two different experiments of SEI formation on freshly deposited Li after 120 min of Li deposition are depicted in red and turquoise. The stiffness histogram of the SEI formed on Li foil soaked in electrolyte for 300 min is displayed in black. The shapes of these histograms differ from those obtained earlier in SEI formation, revealing that the mechanical properties of the SEI change over time. Notably, these changes are similar for both methods of SEI preparation, since the turquoise and black histograms show similar features at the same stiffness values in Fig. 3b and also undergo similar changes compared to their preceding versions (turquoise and black, respectively) in Fig. 3a. However, it should be noted that the time scales for these changes are different between SEI formation on freshly deposited Li compared to SEI formation on Li foil submerged in electrolyte. This is explained by a native passivation layer that might inhibit SEI formation. These results show that the outer layer of the SEI, which is probed by AFM, consists of rather soft mechanical species, as expected for an organic outer layer. For the inner, mostly inorganic layer of the SEI, further influences of the native passivation layer are expected, but cannot be probed by AFM.

The temporal evolution of the mechanical properties of the outer SEI layer is depicted in more detail in Fig. 3c. Here, the stiffness histograms at different durations of Li deposition are depicted for two experiments. Both experiments show that the histogram shape and position vary over time. The histogram positions slightly vary between the experiments. The AFM provides a very local view of the sample, probing an area of 5 μm by 5 μm in these experiments. Hence, the variations of mechanical surface composition occur due to a lateral heterogeneity of the SEI layer.

Nanoindentation

In this section, nanoindentation results with higher indentation depth are reported. Bulk Li was cut using a thin W wire to obtain a pristine Li surface with low roughness and without a natural passivation layer. To compare different passivation layers formed on the Li surface, it was either cut in an argon atmosphere (Ar-cut Li) inside a glovebox or submerged in ethyl methyl carbonate (EMC) solvent (EMC-cut Li). The storage modulus, hardness and loss factor determined through CSM are depicted in Fig. 4b–d for the measurements on Ar-cut Li and EMC-cut Li. The non-transparent lines represent the mean values while the transparent patches represent the minimum and maximum values for the respective indentation depth.

Fig. 4b shows that Ar-cut Li and EMC-cut Li exhibited a sharp decline in storage modulus up to 100 nm for Ar-cut Li and 200 nm for EMC-cut Li. For both, the modulus levels between 6500 MPa and 5000 MPa. These values are in accordance with the literature, where moduli between 1900 MPa and 10 000 MPa are reported for bulk Li, depending on the crystal orientation.[27,28] The initial decrease in modulus is attributed to a wrongly measured indentation depth $h = 0$ (zero-point error)[29] probably because of surface roughness or tip rounding. Zero-point error might have occurred since forces of up to 20 μN were assumed at zero

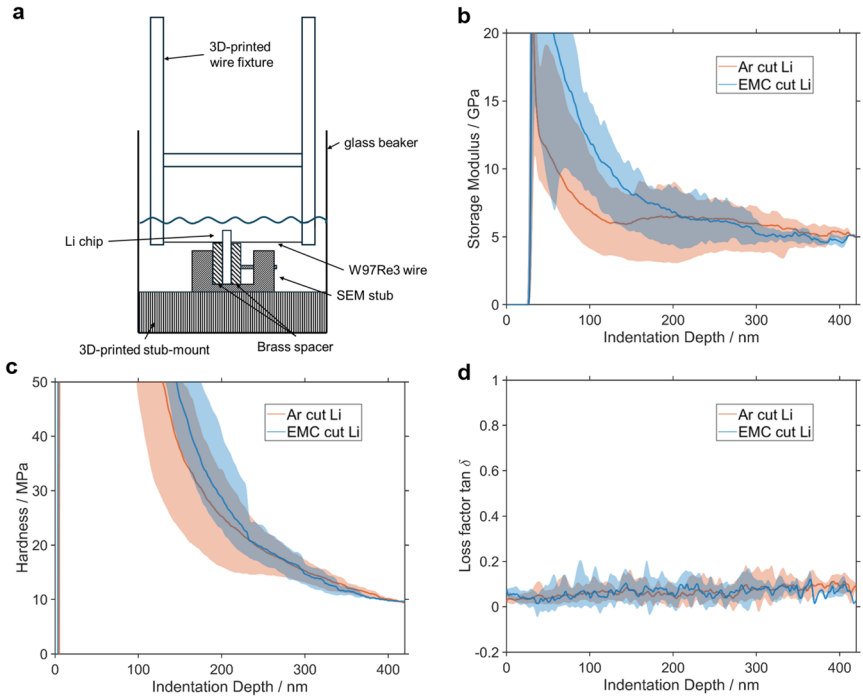

Fig. 4 Li foil cutting with a W wire. (a) The schematic of the setup used for cutting the Li foil. (b) Storage modulus, (c) hardness and (d) loss factor tan δ against the indentation depth using CSM mode for Li cut in argon (orange) and in EMC (blue). The plotted data has been smoothed using a Gaussian-weighted moving average filter to reduce noise but keep the important features.

displacement, which could have led to contact loss during CSM measurements. As shown in Fig. 4c, the hardness continued to decline even after the modulus had levelled out. This was likely caused by the size effect, as has been reported to be a significant factor in lithium.[30] A hardness of 40 MPa was measured at an indentation depth of 150 nm, while a reduced value of 10 MPa was obtained at a depth of 400 nm, and further decreased. A literature value for the hardness of bulk lithium is 2.01 MPa.[28] For the loss factor tan δ depicted in Fig. 4d, the mean value remained between 0 and 0.1 for both Ar-cut Li and EMC-cut Li, while the min and max values remained between 0 and 0.2. Values like this would be expected for lightly cross-linked, glassy and crystalline polymers.[31]

For the storage modulus, the biggest discrepancies occurred at depths below 100 nm where the measurement is likely unreliable, given the increase in modulus in pure lithium. Still, the measured storage modulus of EMC-cut Li at 100 nm was almost double that of pure Li. Hence, it is assumed that a layer of higher hardness and modulus had formed on the Li. Since both sample types showed nearly the same storage modulus for indentation depths greater than 200 nm, while the storage modulus of Ar-cut Li already remained nearly constant after 100 nm, the layer thickness could be assumed to be in the 100 nm range. It is quite likely for the formed layer to be much thinner than in carbonate electrolytes using additional ethylene carbonate (EC) and $LiPF_6$. According to Weber *et. al.*,[32]

an SEI layer thickness of roughly 100 μm is to be expected when Li is left in EC : EMC (1 : 1 by weight) + 1 M $LiPF_6$ electrolyte for 20 min. The solvated ions have been reported to aid the reduction of carbonate solvents.[33] Even if $LiPF_6$ had been present in EMC, the layer would likely still exhibit a smaller thickness, as EMC has a significantly lower dielectric constant than EC and is thus less likely to be coordinated by lithium ions.[34]

Instead of removing the natural passivation layer mechanically, an artificial SEI (ASEI) layer can be created on top of it by treating the Li surface with solutions that form specific reaction products. In this work, we investigated the treatment of Li with two different ILs, namely 1-butyl-1-methylpyrrolidinium difluro(oxolato)borate [$Pyr_{1,4}$][DFOB] for nanoindentation and 1-butyl-1-methylpyrrolidinium bis(fluorosulfonylIimid [$Pyr_{1,4}$][FSI] for AFM.

Electrochemical performance

Fig. 5 shows a comparison of the voltage measured during electrochemical stripping and plating of Li||Li cells, with a current density of 1 mA cm^{-2} at an areal charge of 0.5 mAh cm^{-2}, in LP30 (EC : dimethyl carbonate (DMC) (1 : 1 by volume) + 1 M $LiPF_6$, Sigma Aldrich) electrolyte. Since a full cycle takes exactly 1 h, the cycle time in h is equal to the number of cycles. Both symmetrical cells use the same type of Li chip as the electrodes (16 mm cutout from Honjo Li-metal foil, thickness 500 μm, battery grade). For the blue curve, Li was treated with two drops of 10 wt% Pyr_{14}DFOB in dimethoxyethane (DME) for three days (IL-treated Li) before being assembled into a coin cell; for the orange curve, no treatment was performed before (untreated Li).

Since the symmetrical cells have an open-circuit potential (OCP) of 0 V, the measured potential directly reflects the overpotential from Li stripping and plating.[35] For the coin cells with untreated Li, the overpotential gradually decreased from an absolute value of ≈380 mV in the first step to ≈90 mV in the first 30 cycles. It remained nearly constant until cycle 200. After cycle 200, a near-

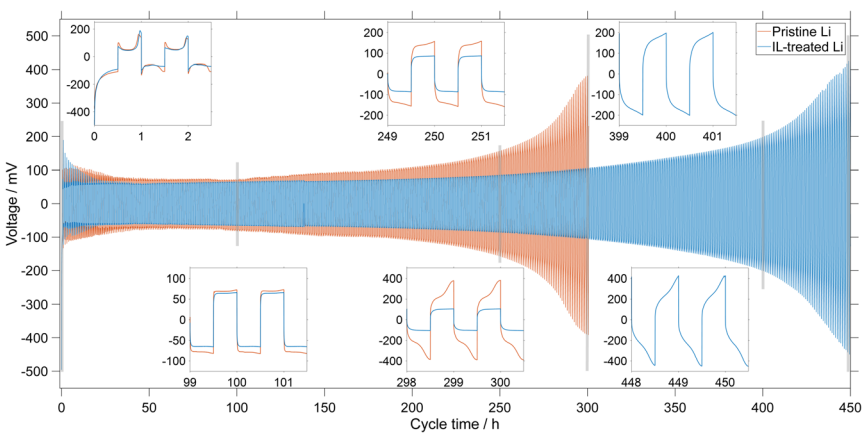

Fig. 5 Voltage during continuous stripping and plating of Li||Li cells with a current density of 1 mA cm^{-2} at an areal charge of 0.5 mAh cm^{-2} in LP30 electrolyte. For the blue curve, Li has been treated with the IL; for the orange curve, no treatment was performed before. Magnified subplots are shown for six 2.5-hour windows corresponding to the positions of the translucent grey lines to visualise the change in voltage curve shape over cycles.

exponential increase up to ≈400 mV at cycle 300 was observed. While the coin cells with IL-treated Li showed a higher absolute overpotential value of ≈500 mV, it decreased even more than that of the untreated Li and remained lower after cycle 10. At cycle 300, the overpotential of the IL-treated Li reached ≈100 mV. It then gradually increased to ≈150 mV at cycle 400. After cycle 400, the overpotential also showed a near-exponential increase up to ≈400 mV at cycle 450. The cycle count to reach 400 mV was therefore around 50% higher for the IL-treated Li in comparison with the untreated Li. An increase in overpotential in a symmetrical Li cell occurs due to an unstable SEI and the formation of "dead" Li. According to the literature, these accumulated layers of "dead" Li would increase ionic resistance in the cell and therefore the overpotential at the same current rate.[36,37] Since an identical electrolyte was used in both cells, it is assumed that the IL-treatment contributes to an artificial SEI (ASEI) as a protective layer on top of the Li. A stiff protective layer might have suppressed dendrite formation, therefore decreasing the surface area and the amount of "dead" Li.

Nanoindentation in ionic liquids

To understand the formed (A)SEI better, nanoindentation of a Li surface, without removal of the natural passivation layer and treated with two drops of $Pyr_{14}DFOB$

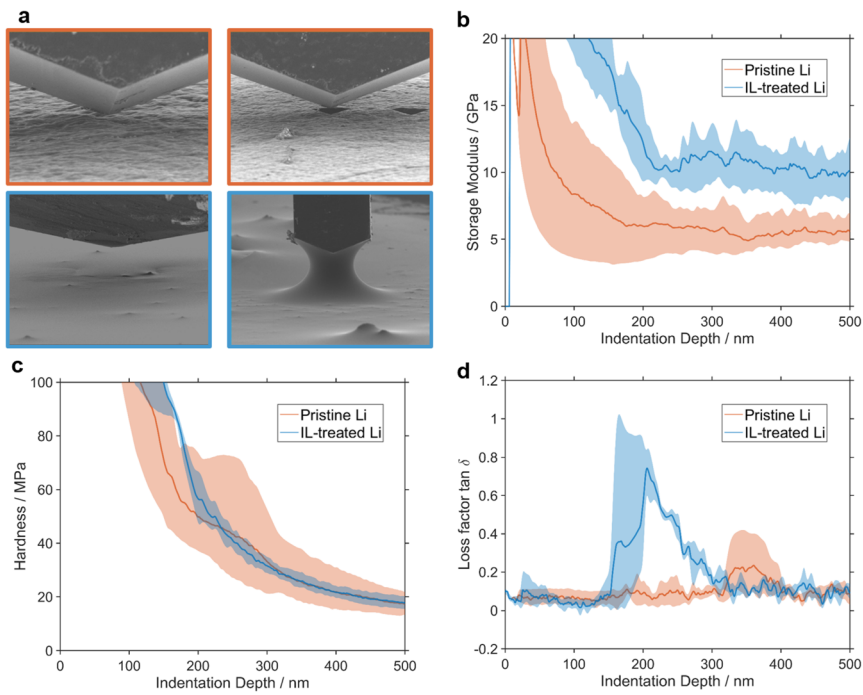

Fig. 6 (a) SEM image of surface morphology of the pristine Li (top, orange contour) and IL-treated Li (bottom, blue contour) before (left) and after (right) nano-indentation. (b) Storage modulus, (c) hardness and (d) loss factor tan δ against the indentation depth using CSM mode for pristine Li (orange) and IL-treated Li (blue). The plotted data has been smoothed using a Gaussian-weighted moving average filter to reduce noise but keep the important features.

in DME for four days before the measurement, was performed and the results are shown in Fig. 6. As can be seen in Fig. 6a, the nanoindenter tip was completely out of contact before and after the indentation into the untreated and rough Li surface. This rough surface led to unstable contact during the initial ≈100 nm and the storage modulus measurement results showed very high initial values, probably due to a zero-point error, as discussed for Fig. 4. This zero-point error can be adjusted for measurements in homogeneous materials, but this is nearly impossible for our measurements of the heterogeneous surface layer.[29] Additionally, for this pristine Li surface, the depth-profiling results exhibited significant stochastic fluctuations in the storage modulus over the first 200 nm of displacement in Fig. 6b. This fluctuation is a sign of the heterogeneous nature of the native passivation layer.[38] The loss factor tan δ in Fig. 6d shows a higher mean value of ≈0.2 and a maximum of ≈0.4 between 300 and 400 nm. Since the minimum value remains around 0, a transition zone was present at this indentation depth for some indents. In contrast, the IL-treated surface shows fewer stochastic fluctuations for the storage modulus between 100 and 200 nm (Fig. 6b). For indentation depths greater than 200 nm, the quasi-constant storage modulus is twice as high for the IL-treated surface (≈8–12 GPa) than for the untreated surface (≈5–7 GPa) which is in the same region as for the cut Li in the previous section and in good agreement with literature values for the corrected elastic modulus of isotropic polycrystalline lithium (≈7.8 GPa) reported by Herbert *et al.*[39] Different to the EMC-cut Li, the ASEI also influences the storage modulus for higher indentation depths.

The hardness shown in Fig. 6c shows a similar trend as for the cut Li samples. Both curves show asymptotically decreasing hardness for increasing indentation depths. Additionally, as for the hardness of cut Li in Fig. 4c, the IL-treated sample shows higher hardness until ≈250 nm and shows nearly the same value for higher indentation depths.

Similar to the loss factor tan δ for cut Li shown in Fig. 4d, the mean value for tan δ remains between 0 and 0.1 for the first 150 nm of indentation depth, also indicating a similar behaviour to lightly cross-linked, glassy and crystalline polymers.[31] For the IL-treated sample, this is followed by a significant spike and a clearly observable broad peak up to a mean value of about 0.8 between 150 and 300 nm indentation depth, signaling the breakthrough of a highly cross-linked sub-layer.[40] The pristine Li did not show a similar peak in tan δ. For the pristine Li, the mean value of tan δ only exceeded 0.1 between about 320 and 400 nm indentation depth, up to a mean value of 0.2. Since no significant changes in storage modulus or hardness could be observed for pristine Li for this indentation depth, the deviation might only have occurred due to a higher maximum value of a single measurement and was therefore not considered an indicator for a cross-linked sub-layer.

On the other hand, the sub-layer formed on the IL-treated sample might be the reason for the increased suppression of dendrite formation shown for Li deposition after IL-treatment of Li surfaces.[6] It could also be observed that the storage modulus (Fig. 6b) remained nearly constant after the maximum value for tan δ which also indicated that the tip indented in bulk Li from then on. Between approximately 200 and 300 nm indentation depth, the loss factor tan δ then decreased linearly with stochastic fluctuations for the IL-treated sample and remained steady around 0.1 until the maximum indentation depth of 500 nm, also indicating that no further cross-linked sub-layer was penetrated for higher indentation depths.

Atomic force microscopy in ionic liquids

The low-indentation-depth regime, which is unstable in nanoindentation experiments, is probed well by AFM in ILs. The mechanical properties of the SEI formed in ILs are studied for Li plated on Ni foil in three IL-based electrolytes. The effect of the additive fluoroethylene carbonate (FEC) and the influence of the concentration of the conduction salt on mechanical properties are evaluated. Two different ratios of IL $Pyr_{14}FSI$ and conduction salt lithium bis(trifluoromethanesulfonyl)imide (LiTFSI) were tested, denoted as 9 : 1 electrolyte and 8 : 2 electrolyte. The 8 : 2 electrolyte was also tested with the addition of 5 wt% FEC additive, denoted as 8 : 2 + FEC electrolyte. The corresponding morphology has been previously published.[41]

The stiffness histograms obtained during the plating process are depicted in Fig. 7. Fig. 7a illustrates the plating process in electrolyte 9 : 1. At open circuit voltage (OCV), the histogram shows a broad peak at about 1600 MPa. Once plating starts, the histogram features a broad peak between 0 and 1000 MPa, which

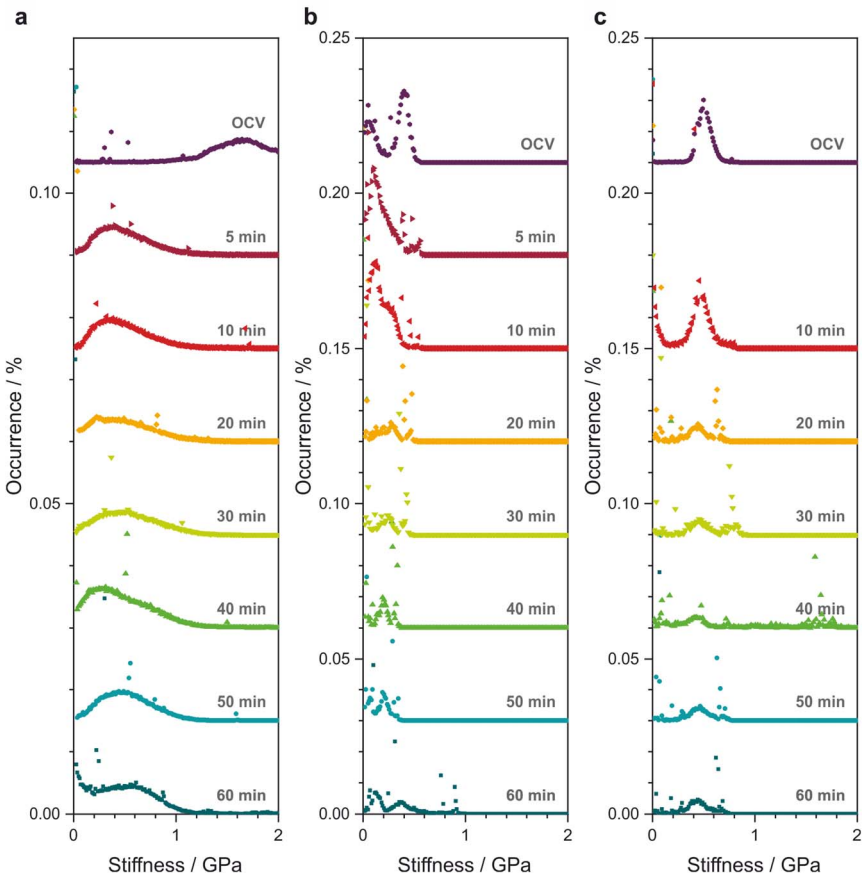

Fig. 7 Evolution of stiffness histograms during lithium plating on Ni foil in electrolytes (a) $Pyr_{14}FSI$ + LiTFSI 9 : 1, (b) $Pyr_{14}FSI$ + LiTFSI 8 : 2, and (c) $Pyr_{14}FSI$ + LiTFSI 8 : 2 + 5 wt% FEC at a current density of 80 μA cm^{-2}. Depicted is the relative occurrence in percent; bin width is 10 MPa. Offsets between histograms are (a) 0.015%, (b) 0.02% and (c) 0.01%.

Table 1 Comparison of AFM and nanoindentation regarding testing conditions, and spatial and depth resolution

	AFM	Nanoindentation
Environment	Flexible (liquid + vacuum)	
Indentation depth	Small	High
Experimental time	Fast	Slow
Spatial resolution	High (nm)	Low (μm)

slightly changes its shape during plating. At the end of plating, an additional peak at stiffness values up to 150 MPa arises.

The stiffness histograms obtained in 8 : 2 electrolyte are presented in Fig. 7b. They are composed of broad peaks between 0 MPa and 1000 MPa. At OCV, the histogram exhibits two distinctive peaks. Upon plating, the histograms consist of several narrow peaks that change their position and intensity over time. Starting from 30 min of plating, the overall shape remains the same; however, the peaks shift both to lower stiffness values and closer together. This indicates that the size of the AFM tip increases, which is assumed constant for stiffness calculations. Thereby, the actual stiffness values are underestimated.

Fig. 7c depicts the histograms of electrolyte 8 : 2 + FEC. The histograms exhibit a main peak that remains constant in its position around 450 MPa. From 20 min of plating, the shapes on the histogram are rather unchanged, featuring several additional peaks with lower intensity.

In comparison, the concentration of the Li salt has a higher impact on the stiffness histograms, reflecting the mechanical composition of the SEI rather than the addition of FEC. Both the histograms obtained in electrolytes 8 : 2 and 8 : 2 + FEC exhibit similar features with a main peak and several narrow peaks next to it. In the 9 : 1 electrolyte, the histograms are very broad with hardly distinguishable individual peak positions. Furthermore, the histograms obtained in the 8 : 2 + FEC electrolyte show the least variation in histogram shape and peak positions. Hence, the FEC additive promotes a mechanically consistent and stable SEI throughout the plating process. This is also reflected in the morphology.[41] To discuss the relation of histogram shape to morphology and dendrite formation in more detail, further experiments are required. Compared to conventional carbonate-based electrolytes (Fig. 3c and ref. 11), the stiffness fingerprints of IL electrolyte 9 : 1 (Fig. 7a) show the greatest similarities considering the histogram shapes. The SEIs formed in IL electrolytes 8 : 2 and 8 : 2 + FEC exhibit distinctly differently shaped histograms with more individual peaks. This illustrates the higher complexity of IL-based electrolytes and resulting reaction products reflected in the SEI compared to carbonate-based electrolytes.

Advantages and comparison of AFM and nanoindentation

Both methods, AFM and nanoindentation, demonstrate individual strengths that complement each other (Table 1). The environment under which both techniques can be performed is determined by the setup. For setups coupled with optical microscopy, liquid, ambient or protective gas environments are feasible. Setups coupled to electron microscopy operate under a vacuum environment. AFM thrives on locally resolved mapping of the surface morphology and contact

stiffness and probes the outermost surface layers, which are not easily accessible by nanoindentation. High sampling rates of less than 0.1 s per force curve and high spatial resolution can be achieved. Nanoindentation, in contrast, performs separate indents, which damage the surface morphology. A wide range of indentation and selective probing of different layers are possible. The technique requires more than 1 s per indent. The lateral resolution is limited by a distance of at least 10 times the indentation depth between the indents to avoid crosstalk. A superimposed oscillation on the indentation allows quasi continuous depth profiling.

Conclusions

In this work, it is demonstrated that both AFM and nanoindentation are excellent methods to study the mechanical properties of the SEI layer. Additionally, both methods complement each other with respect to probing environment, sampling depth, rate and area. Thereby, a multiscale approach greatly enhances the knowledge gained about the studied system. The complementarity of both methods for the SEI formed on Li deposited on a Cu substrate is shown. Furthermore, we present results on the SEI in advanced electrolytes based on ionic liquids. The components contributing to the mechanical surface properties are electrolyte dependent and form independently of the method of SEI formation. The different plastic behaviours of Li and its surface layer have been exploited to estimate layer thicknesses. An advanced nanoindentation mode enables depth-profiling of surface layers.

Author contributions

Beatrice Wolff: conceptualisation, methodology, investigation, data curation, formal analysis, writing the original draft. Sascha Berg: conceptualisation, methodology, investigation, data curation, formal analysis, writing the original draft. Alexander Pinto: investigation, data curation, writing – review & editing. Tobias Sedlatschek: resources, writing – review & editing. Xinlin Li: resources, writing – review & editing. Ziyuan Lyu: investigation, resources, writing – review & editing. Dominik Stępień: resources, writing – review & editing. Christoph Broeckmann: resources, writing – review & editing. Dominic Bresser: resources, writing – review & editing. Rüdiger-A. Eichel: resources, data curation, funding acquisition. Chi-Cheung Su: writing – review & editing. Egbert Figgemeier: resources, validation, supervision, data curation, funding acquisition. Florian Hausen: resources, validation, supervision, data curation, funding acquisition, writing the original draft.

Conflicts of interest

There are no conflicts to declare.

Data availability

Ref. 11, 24 and 41–48 are cited in the supplementary information (SI). Data for this article, including AFM and nanoindentation data, are available at Jülich data

at https://doi.org/10.26165/JUELICH-DATA/OAGLHM. Supplementary information: additional experimental details, information about the exact calibration of both individual methods as well as extended general theory. See DOI: https://doi.org/10.1039/d6fd00045b.

Acknowledgements

This collaborative work has been performed within the LILLINT II research project, jointly funded by the US Department of Energy (DOE) and the German Federal Ministry of Research, Technology and Space (BMFTR). B. W., S. B., R.-A. E., E. F. and F. H. acknowledge financial support under project number 13XP0511B. Z. L., D. S. and D. B. acknowledge financial support under project number 03XP0511E. C.-C .S. and X. L. thank the US DOE, VTO. Argonne National Laboratory is operated by the DOE Office of Science by UChicago Argonne, LLC, under contract DE-AC02-06CH11357. B. W. and F. H. acknowledge Patrick Keister who recorded AFM data of Li deposited on Cu as part of an internship.

Notes and references

1 B. Horstmann, J. Shi, R. Amine, M. Werres, X. He, H. Jia, F. Hausen, I. Cekic-Laskovic, S. Wiemers-Meyer, J. Lopez, D. Galvez-Aranda, F. Baakes, D. Bresser, C.-C. Su, Y. Xu, W. Xu, P. Jakes, R.-A. Eichel, E. Figgemeier, U. Krewer, J. M. Seminario, P. B. Balbuena, C. Wang, S. Passerini, Y. Shao-Horn, M. Winter, K. Amine, R. Kostecki and A. Latz, *Energy Environ. Sci.*, 2021, **14**, 5289–5314.

2 D. Weintz, M. Werres, B. Horstmann, R. Amine, C.-C. Su, X. Li, Y. Xu, R. A. Ahmed, W. Xu, C. Wang, B. von Holtum, S. Wiemers-Meyer, D. Chen, J. Lai, F. Shi, S. Berg, E. Figgemeier, C. O. Plaza-Rivera, D. Wang, Y. Shao-Horn, A. Unni, U. Krewer, S. Scoggins, P. B. Balbuena, J. M. Seminario, A. Sarycheva, Z. Lyu, D. Bresser, F. Hausen, R.-A. Eichel, K. Amine, A. Latz, R. Kostecki, M. Winter and I. Cekic-Laskovic, *Nat. Nanotechnol.*, 2026, **21**, 336–351.

3 X. He, D. Bresser, S. Passerini, F. Baakes, U. Krewer, J. Lopez, C. T. Mallia, Y. Shao-Horn, I. Cekic-Laskovic, S. Wiemers-Meyer, F. A. Soto, V. Ponce, J. M. Seminario, P. B. Balbuena, H. Jia, W. Xu, Y. Xu, C. Wang, B. Horstmann, R. Amine, C.-C. Su, J. Shi, K. Amine, M. Winter, A. Latz and R. Kostecki, *Nat. Rev. Mater.*, 2021, **6**, 1036–1052.

4 Y. Chen, W. Wu, S. Gonzalez-Munoz, L. Forcieri, C. Wells, S. P. Jarvis, F. Wu, R. Young, A. Dey, M. Isaacs, M. Nagarathinam, R. G. Palgrave, N. Tapia-Ruiz and O. V. Kolosov, *Nat. Commun.*, 2023, **14**, 1321.

5 K. Periyapperuma, E. Arca, S. Harvey, T. Pathirana, C. Ban, A. Burrell, C. Pozo-Gonzalo and P. C. Howlett, *ACS Appl. Mater. Interfaces*, 2020, **12**, 42236–42247.

6 C. A. Calderón, A. Vizintin, J. Bobnar, D. E. Barraco, E. P. M. Leiva, A. Visintin, S. Fantini, F. Fischer and R. Dominko, *ACS Appl. Energy Mater.*, 2020, **3**, 2020–2027.

7 S. R. Cohen and E. Kalfon-Cohen, *Beilstein J. Nanotechnol.*, 2013, **4**, 815–833.

8 E. G. Herbert, W. C. Oliver and G. M. Pharr, *J. Phys. D: Appl. Phys.*, 2008, **41**, 074021.

9 J.-L. Li, Y.-N. Wang, S.-Y. Sun, Z. Zheng, Y. Gao, P. Shi, Y.-J. Zhao, X. Li, Q. Li, X.-Q. Zhang and J.-Q. Huang, *Adv. Energy Mater.*, 2025, **15**, 2403845.
10 H.-H. Sun, A. Dolocan, J. A. Weeks, R. Rodriguez, A. Heller and C. B. Mullins, *J. Mater. Chem. A*, 2019, **7**, 17782–17789.
11 B. Wolff and F. Hausen, *J. Electrochem. Soc.*, 2023, **170**, 010534.
12 Z. Zhang, Y. Li, R. Xu, W. Zhou, Y. Li, S. T. Oyakhire, Y. Wu, J. Xu, H. Wang, Z. Yu, D. T. Boyle, W. Huang, Y. Ye, H. Chen, J. Wan, Z. Bao, W. Chiu and Y. Cui, *Science*, 2022, **375**, 66–70.
13 W.-W. Wang, Y. Gu, J.-H. Wang, Z.-B. Chen, X.-T. Yin, Q.-H. Wu, J.-W. Yan and B.-W. Mao, *J. Electrochem. Soc.*, 2022, **169**, 020563.
14 W.-W. Wang, Y. Gu, H. Yan, S. Li, J.-W. He, H.-Y. Xu, Q.-H. Wu, J.-W. Yan and B.-W. Mao, *Chem*, 2020, **6**, 2728–2745.
15 Y. Gao and B. Zhang, *Adv. Mater.*, 2023, **35**, 2205421.
16 Z. Zhang, K. Smith, R. Jervis, P. R. Shearing, T. S. Miller and D. J. L. Brett, *ACS Appl. Mater. Interfaces*, 2020, **12**, 35132–35141.
17 S. Benning, C. Chen, R.-A. Eichel, P. H. L. Notten and F. Hausen, *ACS Appl. Energy Mater.*, 2019, **2**, 6761–6767.
18 V. Kuznetsov, A.-H. Zinn, G. Zampardi, S. Borhani-Haghighi, F. La Mantia, A. Ludwig, W. Schuhmann and E. Ventosa, *ACS Appl. Mater. Interfaces*, 2015, **7**, 23554–23563.
19 Y. Gao, X. Du, Z. Hou, X. Shen, Y.-W. Mai, J.-M. Tarascon and B. Zhang, *Joule*, 2021, **5**, 1860–1872.
20 C. Gong, S. D. Pu, S. Zhang, Y. Yuan, Z. Ning, S. Yang, X. Gao, C. Chau, Z. Li, J. Liu, L. Pi, B. Liu, I. Capone, B. Hu, D. L. R. Melvin, M. Pasta, P. G. Bruce and A. W. Robertson, *Energy Environ. Sci.*, 2023, **16**, 535–545.
21 T. Yan, S. Liu, J. Li, M. Tao, J. Liang, L. Du, Z. Cui and H. Song, *ACS Nano*, 2024, **18**, 3752–3762.
22 R. Garcia and J. R. Tejedor, *Nanoscale Adv.*, 2025, **7**, 6286–6307.
23 X. Li and B. Bhushan, *Mater. Charact.*, 2002, **48**, 11–36.
24 G. Pharr, W. Oliver and F. Brotzen, *J. Mater. Res.*, 1992, **7**, 613–617.
25 H. Shin, J. Park, S. Han, A. M. Sastry and W. Lu, *J. Power Sources*, 2015, **277**, 169–179.
26 E. Peled and S. Menkin, *J. Electrochem. Soc.*, 2017, **164**, A1703–A1719.
27 R. P. Schultz, Lithium: Measurementof Young's Modulus and Yield Strength, *Fermi National Accelerator Lab. (FNAL), Batavia, IL (United States) Technical Report FERMILAB-TM-2191*, 2002.
28 J. Aspinall, D. E. Armstrong and M. Pasta, *Mater. Today Energy*, 2022, **30**, 101183.
29 D. Geng, H. Yu, Y. Okuno, S. Kondo and R. Kasada, *Sci. Rep.*, 2022, **12**, 6391.
30 Y. Wang, D. Dang, M. Wang, X. Xiao and Y.-T. Cheng, *Appl. Phys. Lett.*, 2019, **115**, 043903.
31 J. D. Ferry, *Viscoelastic Properties of Polymers*, John Wiley & Sons, Nashville, TN, 3rd edn, 1980.
32 F. M. Weber, I. Kohlhaas and E. Figgemeier, *J. Electrochem. Soc.*, 2020, **167**, 140523.
33 J. Zhang, J. Yang, L. Yang, H. Lu, H. Liu and B. Zheng, *Mater. Adv.*, 2021, **2**, 1747–1751.
34 D. S. Hall, J. Self and J. R. Dahn, *J. Phys. Chem. C*, 2015, **119**, 22322–22330.

35 Q. Zhang, L. Bo, H. Li, J. Li, T. Li, Z. Tian and R. Qiao, *J. Mater. Chem. A*, 2025, **13**, 2047–2055.
36 S. Matsuda, M. Ono and A. Myojin, *ACS Appl. Energy Mater.*, 2023, **6**, 2524–2530.
37 K.-H. Chen, K. N. Wood, E. Kazyak, W. S. LePage, A. L. Davis, A. J. Sanchez and N. P. Dasgupta, *J. Mater. Chem. A*, 2017, **5**, 11671–11681.
38 E. G. Herbert, S. A. Hackney, N. J. Dudney and P. S. Phani, *J. Mater. Res.*, 2018, **33**, 1335–1346.
39 E. G. Herbert, S. A. Hackney, V. Thole, N. J. Dudney and P. S. Phani, *J. Mater. Res.*, 2018, **33**, 1347–1360.
40 D. E. Mansour, C. Herzog, P. Christöfl, L. Pitta Bauermann, G. Oreski, A. Schuler, D. Philipp and P. Gebhardt, *Polymers*, 2021, **13**, 3328.
41 D. Stępień, B. Wolff, T. Diemant, G.-T. Kim, F. Hausen, D. Bresser and S. Passerini, *ACS Appl. Mater. Interfaces*, 2023, **15**, 25462–25472.
42 A. C. Fischer-Cripps, *Nanoindentation/by Anthony C. Fischer-Cripps.*, Springer New York, New York, NY, 3rd edn, 2011.
43 *Handbook of Mechanics of Materials*, ed. S. Schmauder, C.-S. Chen, K. K. Chawla, N. Chawla, W. Chen and Y. Kagawa, Springer Singapore, Singapore, 2019.
44 R. Lakes, *Viscoelastic Solids*, Taylor & Francis, 1998.
45 S. Verma, P. Sarkar and P. Pant, *J. Mater. Res.*, 2021, **36**, 3436–3444.
46 B. Derjaguin, V. Muller and Y. Toporov, *J. Colloid Interface Sci.*, 1975, **53**, 314–326.
47 R. Reifenberger, *Fundamentals of Atomic Force Microscopy, Part I: Foundations*, World Scientific, New Jersey, 2016.
48 R. Garcia, *Chem. Soc. Rev.*, 2020, **49**, 5850–5884.

